RESEARCH ARTICLE SUMMARY

NEUROSCIENCE

Amygdala ensembles encode behavioral states

Jan Gründemann*†, Yael Bitterman*, Tingjia Lu, Sabine Krabbe, Benjamin F. Grewe, Mark J. Schnitzer, Andreas Lüthi†

INTRODUCTION: Affective or metabolic states, such as anxiety, stress, or thirst, enable adaptations of perception and the selection of appropriate behaviors to achieve safety or homeostasis. Classically, changes in brain states are associated with thalamocortical circuitry and sensory coding. Yet homeostatic and affective states are associated with complex behavioral, autonomic, and hormonal responses, suggesting that state representations involve brain-wide networks, including subcortical structures such as the amygdala. Previously, amygdala function has been studied mainly in the framework of Pavlovian conditioning, leading to the identification of specific circuit elements that underlie associative plasticity at the single-cell and neural-ensemble levels. However, how internal states engage neuronal ensembles in the basal amygdala, a hub for regulating affective, homeostatic, foraging, and social behaviors via widespread connections with many other brain areas, remains unknown.

RATIONALE: The encoding of states governing self-paced behaviors, including foraging or place avoidance, should engage large neuronal populations, evolve on longer time scales (seconds to minutes), generalize across contexts, and lead to differences in sensory processing and action selection. We therefore used a miniature microscope and longitudinal imaging of amygdala neural activity in freely moving mice performing a series of behavioral paradigms in different contexts across multiple days. We thereby tracked neuronal population activity across distinct behavioral paradigms in which mice exhibited distinct modes of behavior manifesting different internal states.

RESULTS: We tracked amygdala neuronal activity across the open-field test, the elevated plus maze test, and a classical Pavlovian fear-conditioning paradigm. During open-field exploration, two large ensembles of basal amygdala neurons antagonistically conveyed information about an animal's corner or center location. This population signature of opposing ensemble activity occurred on a slow time scale (seconds), was evident across consecutive days and paradigms, and predicted transitions from exploratory to non-exploratory, defensive states and vice versa. Notably, amygdala ensemble coding did not align with spatial areas generally thought to correspond to global anxiety states (e.g., the open-field corners and the closed arms of the elevated plus maze) but instead reflected moment-to-moment changes in the exploratory or defensive state of the animal. During fear conditioning, sensory responses of amygdala neuronal populations to conditioned (tone) and unconditioned (shock) stimuli were orthogonal to state encoding, demonstrating that fast sensory responses and slow exploratory state dynamics were separately encoded by amygdala networks. Correlations of neural responses to state transitions were largely conserved across major amygdala output pathways to the hippocampus, nucleus accumbens, and prefrontal cortex.

ON OUR WEBSITE

Read the full article at http://dx.doi.org/10.1126/science.aav8736

CONCLUSION: Our study reveals two large, nonoverlapping functional neuronal ensembles of the basal amygdala representing internal states. The ensembles are anatomically intermingled and encode opposing moment-to-moment states changes, especially regarding exploratory and defensive behaviors, but do not provide a scalar measure of global anxiety levels.

The amygdala broadcasts state signals to a wider brain network, including cortical and subcortical areas. These signals are likely correlated with diverse aspects of brain state, including anxiety, arousal, sensory processing, and action selection. This extends the current concept of thalamocortical brain-state coding to include affective and exploratory state representations in the amygdala, which have the potential to control state-dependent regulation of behavioral output and internal drives. Our findings provide a low-dimensional amygdala population signature as a trackable measure for the state dependency of brain function and behavior in defined neuronal circuits. It remains to be tested whether a maladaptive bias in neuronal state coding in the basolateral amygdala contributes to behavioral and physiological alterations in animal disease models. ■

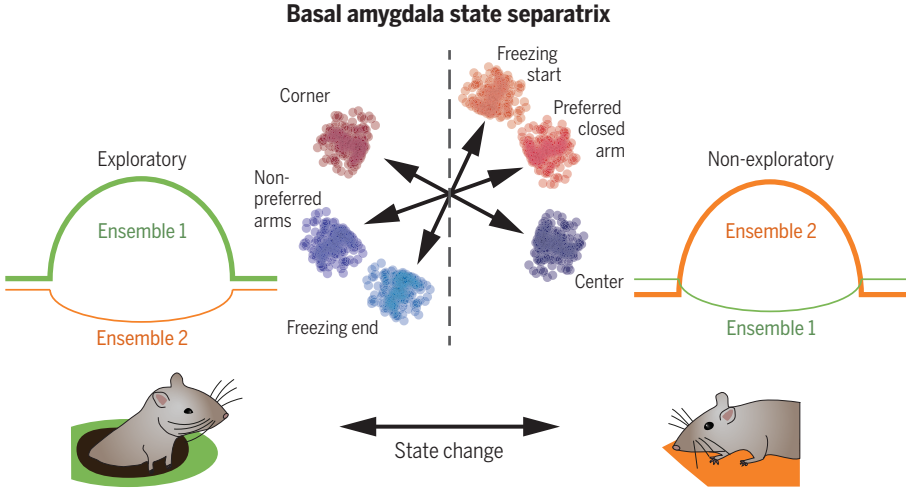

Amygdala ensembles encode behavioral states. Two large, antagonistic basal amygdala neural ensembles signal opposite behavioral states conserved across different behavioral paradigms and contexts. This neural state signature separates exploratory and nonexploratory, defensive behaviors (dashed line) on a moment-to-moment basis, does not align with global anxiety levels (red clusters, high anxiety; blue clusters, low anxiety), is orthogonal to sensory responses, and is broadcast to a wider brain network.

*These authors contributed equally to this work.
The list of author affiliations is available in the full article online.
†Corresponding author. Email: jan.grundemann@unibas.ch (J.G.); andreas.luthi@fmi.ch (A.L.)
Cite this article as J. Gründemann *et al.*, *Science* **364**, eaav8736 (2019). DOI: 10.1126/science.aav8736

RESEARCH ARTICLE

NEUROSCIENCE

Amygdala ensembles encode behavioral states

Jan Gründemann[1,2*†], Yael Bitterman[1*], Tingjia Lu[1], Sabine Krabbe[1], Benjamin F. Grewe[3,4], Mark J. Schnitzer[5], Andreas Lüthi[1,6†]

Internal states, including affective or homeostatic states, are important behavioral motivators. The amygdala regulates motivated behaviors, yet how distinct states are represented in amygdala circuits is unknown. By longitudinally imaging neural calcium dynamics in freely moving mice across different environments, we identified opponent changes in activity levels of two major, nonoverlapping populations of basal amygdala principal neurons. This population signature does not report global anxiety but predicts switches between exploratory and nonexploratory, defensive states. Moreover, the amygdala separately processes external stimuli and internal states and broadcasts state information via several output pathways to larger brain networks. Our findings extend the concept of thalamocortical "brain-state" coding to include affective and exploratory states and provide an entry point into the state dependency of brain function and behavior in defined circuits.

State-dependent adaptations of perception and the selection of appropriate behavioral outputs are essential for an animal's survival (*1*). Changes in internal states have been linked to distinct states of thalamocortical circuitry and sensory coding (*2*–*6*). However, to date, where and how complex internal state changes are encoded as neural state changes have remained elusive. Prior studies identified state-related functions of subcortical (*7*) brain areas and neural circuits (*8*), which can induce rapid shifts in behaviors (*9*–*16*). Homeostatic (hunger and thirst) and affective states induced by aversive or appetitive experience are both associated with perceptual, autonomic, and hormonal responses, which lead to distinct behavioral outputs (*17*–*23*). This suggests that internal states are represented by specific patterns of neuronal activity across large brain networks (*24*). Nevertheless, how ensembles of identified neurons can represent internal states via their activity patterns has remained unknown (*5*, *25*, *26*).

The basolateral amygdala, and specifically its basal nucleus [the basal amygdala (BA)], is a brain hub for regulating affective, homeostatic, and social behaviors. The BA is functionally linked to motor pathways (*27*) that drive specific behavioral outputs, thalamic and cortical sensory areas that process outcome-predicting stimuli (*28*, *29*), and brain centers that sense and regulate behaviorally relevant hormones and neuromodulators (*30*). Previously, amygdala function has been studied mainly in the framework of Pavlovian conditioning (*31*–*34*), leading to the identification of specific circuit elements that underlie associative plasticity at the single-cell (*35*–*37*) and neural-ensemble (*38*) levels. However, we have only a rudimentary understanding of how amygdala neural activity relates to self-paced, state-driven behaviors (*24*), including foraging, risk assessment, and place avoidance (*39*–*41*). These behaviors are strongly driven by internal states (*42*) and may therefore serve as their external manifestations and readouts; yet how ensembles of identified BA neurons encode these states and their relationships to learned stimulus-outcome representations remain unknown.

By using a head-mounted miniaturized microscope (*38*, *43*), we performed deep-brain Ca^{2+}-imaging studies of large populations of BA principal neurons in mice that engaged in a series of behavioral paradigms. This experimental design allowed us to longitudinally track large ensembles of individual neurons to record assumption-free normalcy of neuronal activity (fig. S1) across several days and paradigms.

Results

Amygdala activity during open-field exploration

We used a miniature fluorescence microscope (Fig. 1A and fig. S1, A to D) to track the relative changes in Ca^{2+} fluorescence in large populations of BA principal neurons [calcium/calmodulin-dependent protein kinase II (CaMKII)–positive as well as projection-specific neurons (fig. S8)] in freely moving mice within three different, consecutive behavioral assays (Fig. 1B and fig. S1). We chose these assays because they prompt mice to exhibit distinct modes of behavior that are likely outward manifestations of different internal states.

During the open-field (OF) test, mice generally spent most time in the periphery of the OF (*44*–*47*) (Fig. 1D) (time in the periphery, 76 ± 3%; time in the center, 24 ± 3%; $P < 0.0001$, Wilcoxon matched-pairs signed-rank test; $n = 25$ mice). Nevertheless, mice typically exhibited pronounced exploratory behavior in the OF (Fig. 1G and fig. S2G). They covered large distances (45 ± 2 m in ~10 min; $n = 25$ mice) (Fig. 1C) and ventured out of the corners, along the walls (time in corners, 34 ± 2%; time at walls, 42 ± 1%; $P < 0.01$, Wilcoxon matched-pairs signed-rank test; $n = 25$ mice), and into the center (Fig. 1D).

We tracked the somatic Ca^{2+} activity of BA CaMKII-positive principal neurons (133 ± 6 neurons per animal; $n = 9$ mice) throughout OF exploration (Fig. 1A and fig. S1). BA neurons exhibited diverse activity patterns that included discrete Ca^{2+} transient events as well as slow changes in Ca^{2+}-related fluorescence (Fig. 1H). The average spatial response patterns of individual BA neurons in the OF arena ranged from seemingly nonspecific to area-biased activity that preferentially occurred when the mouse was either in the arena corners (corner-modulated cells) or in the center (center-modulated cells) (Fig. 1I).

We quantified the area bias of the neuronal responses on the basis of the differential Ca^{2+} activity between corners and centers (area score) (see methods). We defined neurons with scores exceeding a selected threshold as area modulated (total proportion of area-modulated neurons, 28 ± 5%) (Fig. 2, A and B). The distribution of area scores on the basis of differential activity in corners versus centers was significantly wider than that of area scores on the basis of neutral divisions of the OF (e.g., left versus right or top versus bottom) or datasets in which we temporally shifted the cellular activity traces relative to the behavioral time course (fig. S2a) (see methods). Accordingly, a substantial fraction of corner- versus center-based area scores was outside of the 95% confidence interval of the neutral left-versus-right (17%) or top-versus-bottom (21%) distributions, as well as the temporally shifted controls (21 ± 3% for 100 random temporal shifts), indicating that the extent of corner-versus-center coding in BA ensembles is significantly greater than that expected from the random fluctuations in the cells' activity patterns. Across the population, comparable proportions of cells were preferently active in the corners or in the center (corners, 13 ± 3% of BA principal neurons per animal; center, 15 ± 3%; $P = 0.641$, Wilcoxon matched-pairs signed-rank test; $n = 9$ mice) (Fig. 2C). Corner-modulated and center-modulated neurons were spatially intermingled in the BA, with no apparent local clustering (Fig. 2, D and E, and fig. S2B).

[1]Friedrich Miescher Institute for Biomedical Research, Maulbeerstrasse 66, Basel, Switzerland. [2]Department of Biomedicine, University of Basel, Klingelbergstrasse 50-70, Basel, Switzerland. [3]Institute of Neuroinformatics, University and ETH Zürich, Winterthurerstrasse 190, Zürich, Switzerland. [4]Department of Electrical Engineering and Information Technology, ETH Zürich, Switzerland. [5]Howard Hughes Medical Institute, CNC Program, James H. Clark Center for Biomedical Engineering and Sciences, Stanford University, Stanford, CA, USA. [6]University of Basel, 4000 Basel, Switzerland.
*These authors contributed equally to this work.
†Corresponding author. Email: jan.grundemann@unibas.ch (J.G.); andreas.luthi@fmi.ch (A.L.)

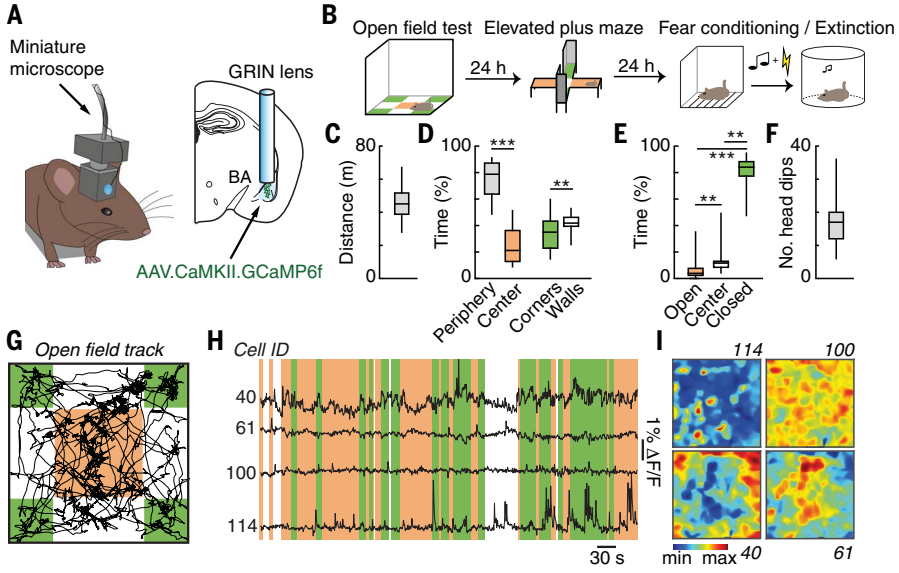

Fig. 1. Deep-brain imaging of BA activity in freely exploring mice. (**A**) Scheme of gradient index lens implantation and virus expression strategy. [The brain image is reproduced from (*83*)] (**B**) Scheme of 7-day behavioral paradigm, including consecutive OF and EPM tests, as well as 5-day FC and fear extinction paradigms (see also Fig. 5). (**C**) Distance traveled in the OF (n = 25 mice). (**D**) Time spent in the center versus the periphery and subareas of the periphery (walls versus corner). $^{**}P < 0.01$, $^{***}P < 0.001$, Wilcoxon matched-pairs signed-rank test (n = 25 mice). For definition of locations, see (G). (**E**) Time spent in the open and closed arms, as well as the center, of the EPM (n = 25 mice). (**F**) Average number of head dips on the EPM (n = 25 mice). (**G**) Example OF track of an individual mouse. Context size, 40 cm by 40 cm. (**H**) Example Ca^{2+} signals of four simultaneously recorded individual cells during OF exploration. Colors indicate mouse location: orange, center; green, corner. $\Delta F/F$, change in calcium-dependent fluorescence. (**I**) Mean Ca^{2+} signal across the OF arena for the four example cells shown in (H), demonstrating nonspecific (cells 114 and 100) and area-modulated (cells 40 and 61) activity patterns. The color bar indicates the cell-by-cell normalized z-score. Box-and-whisker plots indicate the median, the interquartile range, and the minimum to maximum values of the data distribution.

To examine neuronal response dynamics during an animal's transition from the OF center into a corner and vice versa, we averaged neuronal Ca^{2+} responses aligned on crossings of the corner boundary according to the directionality of the transition. This analysis revealed that a large group of BA neurons was either activated (27 ± 4%) (ensemble 1) or inhibited (29 ± 4%) (ensemble 2) (P = 0.641, Wilcoxon matched-pairs signed-rank test; see methods for details on the cluster-based analysis of relative changes in Ca^{2+} fluorescence) upon spatial transitions into or out of the corners (Fig. 2, F and G). The sign of the response of the respective BA ensemble was inverted when the animal exited the corner area, notwithstanding similar speed profiles for the two transitions (Fig. 2, G and H, and fig. S2J). Generally, ensemble 1 cells were activated upon corner entry and overlapped with corner-modulated cells, whereas ensemble 2 cells were activated at corner exits and corresponded to center-modulated cells (Fig. 2F and fig. S2, C to F). The activity patterns of corner- and center-modulated cells were linked to the spatial location or the transition therein and did not depend on differences in average corner and center movement (fig. S2G), general speed correlations on the single-cell level (fig. S2H), or correlations of neuronal activity with instantaneous changes in speed (Fig. 2, G to I, and fig. S2, I and J). Although BA neurons can be speed modulated, speed modulation alone cannot explain the prominent area coding.

We trained a support vector machine classifier (see methods) to test whether corner versus center locations of the animal could be accurately predicted solely on the basis of BA population activity. The classifier reached high decoding accuracies of 86 ± 2%, whereas decoder performance dropped if the decoder was trained and tested on temporally shuffled neuronal data (46 ± 4%; P = 0.004, Wilcoxon matched-pairs signed-rank test) (fig. S2K) or temporally shifted to control for local structures in the behavioral and neuronal data (fig. S2L) (see also methods).

Next, we tested the extent to which corner and center coding was stable across days by using an OF re-exposure paradigm. Area scores of individual neurons were significantly correlated (correlation coefficient r = 0.57; $P < 0.001$) across days, and cells typically did not switch area coding categories, indicating the stability of BA area coding (fig. S3, A and B). Additionally, repeating a similar analysis for the complete longitudinal paradigm, we found that the spontaneous spatial activity map of BA corner (periphery) and center ensembles was stable across different context shapes and that area scores were highly correlated (fig. S3, C and D).

Lastly, we probed whether corner- and center-cell signaling is dependent on the state of the animal or merely on location. Corner-cell location-specific activity was lost when the animals were in a nonexploratory, freezing state in the corners during the fear-conditioning (FC) session (fig. S4, A and B), as well as upon spontaneous or cued freezing in the periphery (fig. S4C). However, using interanimal variability of center exploration as a behavioral proxy of an animal's global anxiety level, we found that BA corner- and center-cell proportions did not correlate with OF center times, suggesting that the relative strength of corner- and center-cell coding is independent of an animal's global anxiety level (fig. S4D).

Amygdala encoding of elevated plus maze exploration

To investigate whether general principles of BA population coding apply to exploratory behavior across different contexts, we imaged the same BA principal neurons during elevated plus maze (EPM) exploration (Figs. 1B and 3B and fig. S1E). Mice spent more time in the closed arms of the EPM (time in closed arms, 81 ± 2%). Typically, one of the closed arms, the preferred home-base arm, was substantially more frequented (fig. S5, A to D). Mice also exhibited exploratory behavior on the EPM. They ventured out of the closed arms into the center (relative time spent, 13 ± 2%) or onto the open arms (6 ± 1%; $P < 0.0001$, Friedman test) (Fig. 1E). Furthermore, the animals performed so-called head dips, characterized by brief periods of visual investigation over the edges of the EPM open arms (Fig. 1F).

Next, we asked whether the area-modulated responses of BA principal neurons that we observed in the OF would generalize to the EPM. Specifically, we hypothesized that enclosed, potentially safe areas are similarly represented between the two paradigms, such that corner-modulated cells might be more active during an animal's stay in the closed arm of the EPM whereas center-modulated cells might show higher activity levels during open-arm exploration. The average activity of corner-modulated cells was reduced in the preferred closed arm (mean z-score, −0.22 ± 0.03; n = 9 animals) (Fig. 3, B and E), whereas center-modulated cells exhibited increased activity in the preferred closed arm (mean z-score, 0.15 ± 0.04; $P < 0.01$, Wilcoxon matched-pairs signed-rank test) (Fig. 3, C and E). Once the animal ventured out of its preferred closed arm to explore the EPM, the average activities of corner- and center-modulated cells reversed such that corner-modulated cells increased their Ca^{2+} fluorescence in the center (Δz-score, 0.246 ± 0.04), less-frequented closed arm (Δz-score, 0.262 ± 0.04), or open arms (Δz-score, 0.222 ± 0.03) whereas center-modulated cells decreased their activity in the respective areas (Δz-score for center, −0.177 ± 0.04; for less-frequented closed arm, −0.183 ± 0.05; and for open

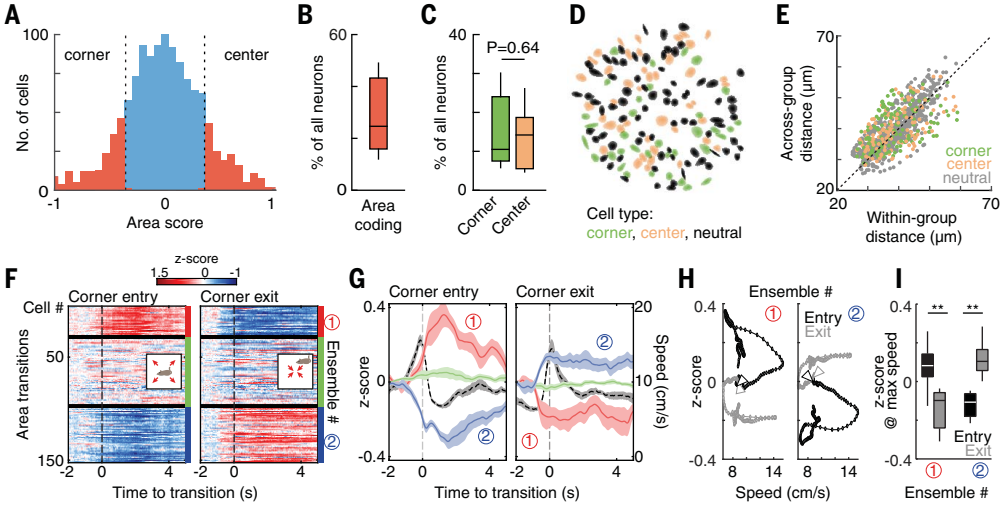

Fig. 2. Large, intermingled populations of BA neurons are spatially modulated. (**A**) Area score histogram of amygdala projection neurons (n = 1201 neurons). Cutoff scores for corner- and center-modulated cells were set at ±1 standard deviation (dashed lines). (**B**) Proportion of area-coding neurons. (**C**) Proportions of corner- and center-modulated neurons are similar (P = 0.64, Wilcoxon matched-pairs signed-rank test). (**D**) Spatial distribution of corner (green)– and center (orange)–modulated cells of one example mouse. Black, neutral cells. (**E**) Mean within- and across-group distances of individual corner- and center-modulated cells (one point per cell). (**F**) Mean responses of functionally clustered groups of individual neurons upon corner-entry (left) and -exit (right) transitions (n = 152 neurons from one mouse; number of entries, 24; number of exits, 21). Zero marks corner-entry or -exit times; responses were baselined on 2 to 1.5 s before transition (see methods). Cells were ordered according to k-means clustering on the average corner-entry response of each cell. Cell identifiers (IDs) were kept identical for corner-exit responses. (**G**) Average corner-entry (left) and -exit (right) responses of corner entry–activated (red) (ensemble 1), –neutral (green), or –inhibited (blue) (ensemble 2) clusters across animals. Black traces indicate the average speed profile upon corner entry or exit. Lines indicate the average across animals ± SEM. (**H**) The Ca^{2+} activity in relation to corner-entry (black) and -exit (gray) transition speeds for the two ensembles (average response profile) reveals that the relationship between instantaneous speed and cellular activity is destination dependent and not solely speed driven. Triangles mark the transition start. (**I**) Average z-score at maximum velocity (ensemble 1, P = 0.008; ensemble 2, P = 0.004; Wilcoxon matched-pairs signed-rank test). The spatial decoding accuracy of corner and center locations in actual and time-shuffled data is shown (P = 0.004, Wilcoxon matched-pairs signed-rank test). Box-and-whisker plots indicate the median, the interquartile range, and the minimum to maximum values of the data distribution. All data are generated from n = 9 animals. **P < 0.01.

arms, −0.156 ± 0.05; all P < 0.01, Wilcoxon matched-pairs signed-rank test) (Fig. 3, D to F). This suggests that the activity of corner-modulated cells correlates with the exploration of the nonpreferred closed and open arms of the EPM. Consistent with this notion, the animals' behavior in the OF corners was not passive but rather characterized by constant activity, exploration, and rearing (figs. S2G and S5E).

To test this idea further, we analyzed the activities of corner- and center-modulated cells during open-arm head dips, a classic exploratory, low-anxiety behavior (*48*). On average, the animals performed 18 ± 2 head dips per EPM session. During head dips, corner-modulated cells were strongly activated (z-score, 0.28 ± 0.04) whereas center-modulated cells were inhibited (z-score, −0.23 ± 0.08; P < 0.01, Wilcoxon matched-pairs signed-rank test) (Fig. 3, G to I). The opposing activation pattern for corner- and center-modulated cell ensembles is preserved during head dips, an alternative, stationary exploratory behavior.

Consistent encoding of behavioral states in amygdala ensembles

Next, we asked how behavioral states and the transitions between them are encoded on the neuronal population level. We extended the analysis to follow the modulation of BA ensemble activity across different states and behavioral paradigms. We classified the neuronal ensembles on the basis of their responses during transitions into the corners of the OF into activated (ensemble 1, or corner-entry activated, 27 ± 4% of all neurons), neutral (transition neutral, 44 ± 3%), or inhibited (ensemble 2, or corner-exit activated, 29 ± 4%) neurons (Fig. 4A; see also Fig. 2G). The activated and inhibited ensembles showed on average inverted relative changes in Ca^{2+} fluorescence upon corner exit (Figs. 2G and 4, A to C). We analyzed the activity of these three ensembles aligned on different behavioral transitions by using the same cluster partition. Consistent with the idea that ensemble 1 neurons encode a general state associated with exploratory behavior across animals, ensemble 1 cells were activated not only upon OF corner entries but also upon open-arm head-dip behavior (Fig. 4, A to C; see also Fig. 3, G to I). By contrast, ensemble 2 neurons exhibited the inverse pattern of activity modulation (Fig. 4, A to C). Notably, when this analysis was extended to freezing behavior (see Fig. 5A), a well-studied, distinctive defensive behavior induced by auditory FC, ensemble 1 and ensemble 2 neurons showed opposite activity changes when animals transitioned into a high-fear, freezing state and upon termination of freezing (Fig. 4A) (methods).

Because ensemble responses were averaged across many neurons (44 ± 3 cells per cluster), we verified that similar results are obtained for single-neuron responses by using an alternative response correlation measure. Single-neuron responses were aligned to the same behavioral transitions used for the ensemble analysis, and pair-wise correlation between responses to a pair of behaviors was calculated across the entire neuronal population. Single-neuron responses to corner entry and corner exit were highly negatively correlated (r = −0.84; P < 0.001) (Fig. 4D). Correlations between single-neuron responses to corner entry, freezing end, and head dips were highly positive, whereas the correlations between responses to freezing start and corner-exit behaviors were significantly negative (Fig. 4E). These correlations were independent of the behavioral session (i.e., freezing during habituation or fear extinctions 1 and 2) (Fig. 4E).

Orthogonal behavioral and sensory coding in BA neuronal ensembles

Next, we tested how the population coding of behavioral states in BA neurons relates to the population coding of sensory stimuli during the acquisition and extinction of classical Pavlovian FC. During conditioning, we paired a previously neutral pure tone [conditioned stimulus (CS); a 75-dB pure tone] with a mild electrical foot shock [unconditioned stimulus (US); 2-s 0.65-mA AC] (see methods). After conditioning, the animals showed increased freezing responses toward the US-paired CS (CS+), which extinguished upon repeated re-exposure to the CS+ (Fig. 5A). BA neurons were about two times more likely to respond to the US (57 ± 3% of all neurons, including excitatory and inhibitory responses; n = 9 animals) (fig. S6, A to C) than to the conditioned stimuli (30 ± 3% of all neurons; n = 9 animals; P = 0.004, Wilcoxon matched-pairs signed-rank test)

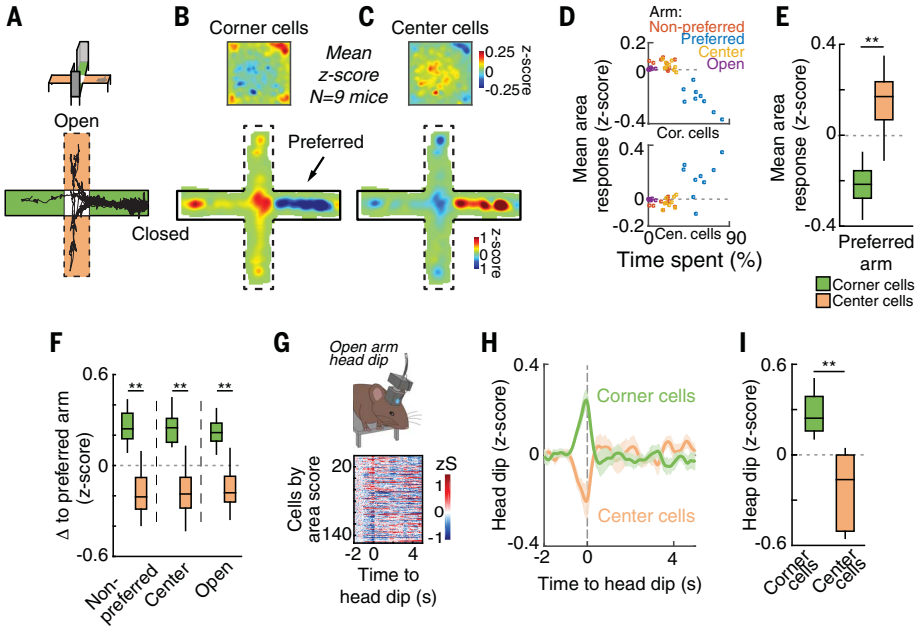

Fig. 3. Corner- and center-modulated cells encode exploratory behavior. (**A**) EPM behavior of the example animal shown in Fig. 1. Green areas represent closed arms, and orange areas represent open arms. (**B**) Average spatial Ca^{2+} activity map of OF corner- and center-modulated cells in the OF (top) and on the EPM (bottom) across animals. (**C**) Average spatial Ca^{2+} activity map of center- and corner-modulated cells in the OF (top) and on the EPM (bottom) across animals. Animals typically had a preferred closed arm, and EPM maps were rotated such that the most frequented closed arm is aligned on the right [arrow in (B)]. (**D**) Mean area responses in the preferred closed arm (blue), nonpreferred closed arm (red), EPM center (yellow), and open arms (purple) for the corner (cor.) (top) and center (cen.) (bottom) cells in relation to the relative time spent at each location. The mean spatial activities in relation to the time spent at the locations are inverted for corner- and center-modulated cells. (**E**) Average preferred-arm responses of corner and center cells (**P < 0.01, Wilcoxon matched-pairs signed-rank test) [(B) to (F) are based on non–time-normalized data]. (**F**) Response difference (Δ) for nonpreferred arms and open arms, as well as the center, compared with the preferred, home-base arm for corner- and center-modulated cells (**P < 0.01 for all comparisons, Wilcoxon matched-pairs signed-rank test). (**G**) Illustration of head-dip behavior on EPM open arms (top) and example BA responses to head dips for 152 simultaneously recorded cells of one animal (bottom). Cell IDs are sorted by area score (see also Fig. 2A). zS, z-score. (**H**) Average responses of corner- and center-modulated cells upon EPM head dips. (**I**) Quantification of the peak response shown in (H) (**P < 0.01, Wilcoxon matched-pairs signed-rank test). Box-and-whisker plots indicate the median, the interquartile range, and the minimum to maximum values of the data distribution. All data are generated from n = 9 animals.

(for selection criteria, see methods) and were more likely to be activated by the CS+ than by a control CS that was not paired with the US (CS–) (CS+, 25 ± 3%; CS–, 8 ± 1%; P = 0.004, Wilcoxon matched-pairs signed-rank test) (fig. S6D).

We classified neurons according to the evolution of their CS+ responses upon FC and fear extinction by using a supervised clustering approach (Fig. 5A and fig. S6A) (see methods). We found functionally distinct CS plasticity subtypes of BA principal neurons that were characterized by differential changes of CS+ responses during FC and extinction—for example, CS-down neurons (those for which the CS response decreased), fear neurons, extinction neurons, and extinction-resistant neurons (Fig. 5A and fig. S6, A and E). None of these CS plasticity subtypes were correlated with either of the behavioral state–related neuronal ensembles (fig. S7A), indicating that experience-dependent CS representations are maintained across different behavioral states.

US responses were dynamic upon FC (Fig. 5B). Across the five CS-US pairings, a supervised cluster analysis (fig. S6B) identified different subtypes of US-excited neurons [32 ± 2% of all neurons, including those with stable US response activity (US-stable), those for which the response decreased (US-down), and those for which the response increased (US-up), as well as post-US neurons] and US-inhibited neurons [25 ± 2% of all neurons, including those with a stable inhibitory response and those for which the inhibitory response was decreased; compared with US-excited neurons, P = 0.129, Wilcoxon matched-pairs signed-rank test] (fig. S6, F and G). Despite the detailed classification of highly diverse and dynamic response patterns to the CS and US across the entire population of BA principal neurons, no significant overlap between individual CS and US plasticity subtypes was observed (figs. S6H and S7, A and C; see also Fig. 4). Notably, US responses per se were not correlated with and were orthogonal to any of the tested behavioral states (Fig. 5C and figs. S6I and S7, B and C), indicating that US representations are not specifically associated with a particular behavioral state.

Before FC and after fear extinction, the population-level CS+ response was not correlated with exploratory or freezing behaviors, which is consistent with the neutrality of the CS+ response at these time points. After FC, the CS+ population response was weakly correlated with exploratory, low-anxiety behaviors (corner entries, freezing end, and head dips) (Fig. 5C). The CS– response followed the same pattern of correlations with behavior as the CS+ response, yet only correlations between the CS– responses after FC and freezing end were significant across animals. After FC, more CS+-responsive neurons overlapped with freezing start–inhibited neurons (32 ± 5%), which are typically activated by exploratory behaviors (similar to ensemble 1) (see Fig. 4), than with freezing start–activated neurons [18 ± 4%, similar to ensemble 2; P = 0.029, Friedman test (P = 0.03, F = 6.89) with post hoc Dunn's multiple-comparison test] (Fig. 5, D and E; for US, see fig. S7B).

Lastly, we tested the hypothesis that the BA would transmit distinct behavioral state– or sensory-related representations to select downstream targets, including the ventral hippocampus (vHC), the medial prefrontal cortex (mPFC), or the nucleus accumbens (NAc). Although some specialization could be observed for individual pathways [typically CS-US coding related (*49*)], the population correlations with behavioral states were largely maintained across output pathways (fig. S8), suggesting that the BA broadcasts state-related signals to larger brain networks.

Discussion

Our study reveals a coding principle of internal state representations in large, functional ensembles of BA neurons (fig. S9). By longitudinal imaging with a miniature microscope and three complementary analytic approaches across multiple paradigms in freely moving animals, we demonstrate large-scale opposing activity dynamics in two functionally distinct, anatomically intermingled ensembles of amygdala neurons that code for distinct behavioral states. This trackable neural population signature of state coding in amygdala ensembles was consistent across different behavioral paradigms and predicted transitions from exploratory behavior to nonexploratory defensive behavior and back.

During OF exploration, a large fraction of BA neurons conveyed area-modulated information about an animal's corner or center location. Notably, such areas are generally thought to correspond to the animal's global anxiety or stress levels (*45*, *50*–*52*). In this classical interpretation, anxious animals would spend most of the time in the corners of the OF or in the closed arms of the EPM. The administration of anxiolytics

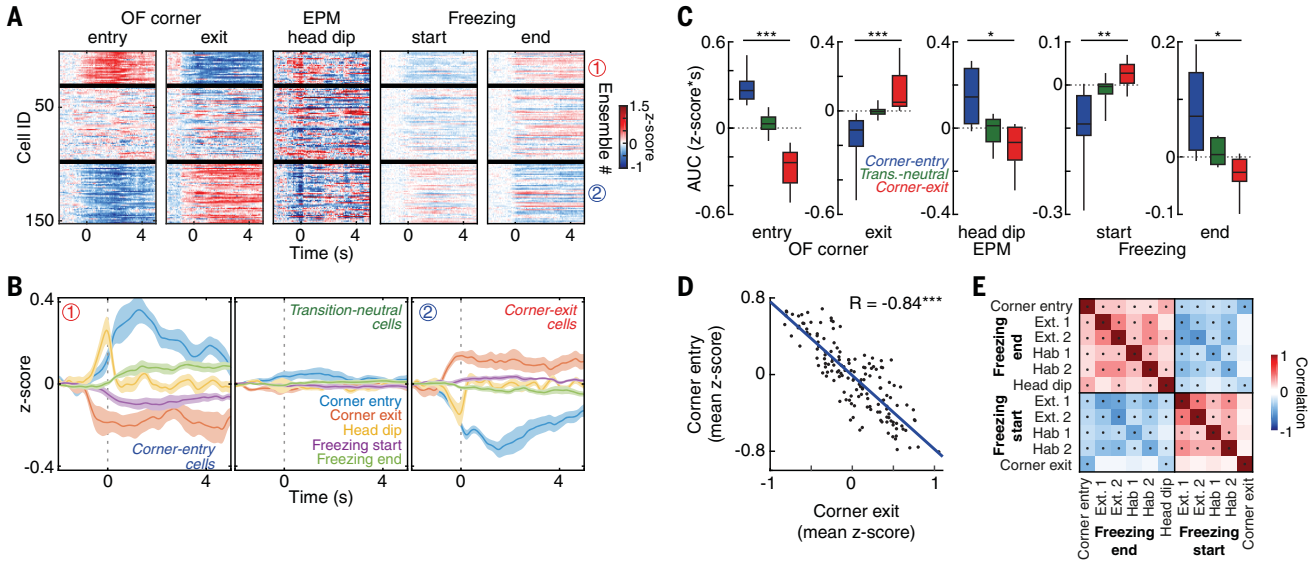

Fig. 4. State coding of BA neuronal ensembles across behavioral paradigms. (**A**) Average response patterns of OF corner entry and corner exit, EPM head dips, and freezing start as well as freezing end for cells clustered on the basis of OF corner-entry responses (top). (**B**) Average cluster response across animals. (**C**) Quantification of the average cluster responses aligned to OF corner entry [*z*-score, corner-entry cells (ensemble 1) = 0.28 ± 0.04; transition-neutral (trans.-neutral) cells = 0.03 ± 0.02; corner-exit cells (ensemble 2) = −0.27 ± 0.05] ($P < 0.001$ for corner-entry cells versus transition-neutral cells), to corner exit (corner-entry cells = −0.16 ± 0.05, transition-neutral cells = −0.003 ± 0.01, corner-exit cells = 0.11 ± 0.04; $P < 0.001$ for corner-entry cells versus transition-neutral cells), to EPM head dips (corner-entry cells = 0.15 ± 0.04, transition-neutral cells = -0.01 ± 0.02, corner-exit cells = -0.09 ± 0.03; $P = 0.014$ for corner-entry cells versus corner-exit cells), and to freezing start (corner-entry cells = −0.09 ± 0.03, transition-neutral cells = −0.01 ± 0.01, corner-exit cells = 0.03 ± 0.01; $P = 0.003$) as well as freezing end (corner-entry cells = 0.08 ± 0.02, transition-neutral cells = 0.01 ± 0.01, corner-exit cells = −0.03 ± 0.01; $P = 0.020$, all Friedman test with post hoc Dunn's multiple-comparison test). *$P < 0.05$; **$P < 0.01$; ***$P < 0.001$. (**D**) Single-cell correlation of corner-entry and corner-exit responses of one example animal ($n = 152$ cells, $r = -0.84$, $P < 0.001$). (**E**) Average correlation matrix of single-cell responses across different behavioral paradigms (dots indicate a significant difference of the correlation from 0 across animals by a one-sample *t* test). Ext., extinction; hab., habituation. Box-and-whisker plots indicate the median, the interquartile range, and the minimum to maximum values of the data distribution. All data are generated from $n = 9$ animals.

reduces global anxiety levels and increases OF center times, as well as EPM open-arm times, while foot shock–induced freezing is reduced (*53*–*56*). If BA ensembles track global anxiety, this would suggest a model where BA activity is similar during center entries, in EPM open arms, and at freezing start or, vice versa, similar during corner entries, in EPM closed arms, and at freezing end. The amygdala would act as an anxiometer, or anxiety classifier (fig. S10A). However, the two large opposing BA ensembles that we identified do not align with this expectation but rather reflect moment-to-moment changes in the exploratory state of the animal, suggesting that the animal's exploratory state is the most parsimonious, common denominator of the observed ensemble activity (fig. S10B). Nevertheless, moment-to-moment changes in exploratory behavior are likely to be correlated with relative changes in different aspects of brain state, including anxiety, arousal, sensory processing, and action selection. We found that the location-specific activity of corner cells is stable across days and contexts. Nevertheless, it is eliminated and even reversed in high-fear, freezing states, indicating that BA ensembles are not encoding spatial location per se.

State changes manifest in changes of behavioral outputs, which inherently affect an animal's motion and speed. Nevertheless, the observed neural state signatures cannot be explained exclusively by changes in the movement parameters of the animal. Each individual state ensemble (e.g., corner-in versus corner-out) contained a large number of non–speed-correlated cells as well as similarly sized subsets of positively and negatively speed-correlated cells. Yet, upon spatial transitions (e.g., corner entry), within-ensemble activity was homogenous and direction selective, while being independent of transition speed. Furthermore, state ensemble coding was similar in stationary (e.g., head-dip and stretch-attend) and nonstationary exploratory behaviors. The target location of the movement or the exploratory character of distinct stationary behaviors dominated the speed modulation of individual subsets of cells. This rules out the possibility that the discovered state ensembles were solely motion related. Our findings in freely moving animals extend the concepts of cortical state coding classically related to movement- and arousal- or attention-associated processes in the brain state (*57*–*63*) toward dynamic exploratory and affective state representations by large neural ensembles in subcortical circuits that may include diverse patterns of physiological, sensory, and locomotion processes.

Consistent state-dependent changes in the activity of single cells suggest a fixed-state ensemble membership of individual neurons and a homogenous, state-dependent regulation of individual neuron activity within a given state ensemble. Changes in population activity were characterized by slow (seconds-long), continuous dynamics in defined ensembles and aligned with behavioral transitions, reminiscent of a potential amygdala attractor network state, previously suggested to underly internal states (*24*). Slow changes in amygdala ensemble activity that emerged as a basic structure on the population level were predictive of changes in exploratory behaviors across days and paradigms (fig. S11). Such slow regulation of antagonistic BA ensemble activity might involve state-dependent changes in input activity, neuromodulation, and local circuit mechanisms (*64*–*67*) and can now be tested for generality in other freely moving behavioral paradigms.

Similar to previous studies, we found different types of CS-plastic neurons upon FC and extinction (*35*, *36*, *38*, *68*, *69*). Despite being encoded by amygdala neuronal populations (*38*), sensory responses were correlated only partially (CS) or not at all (US) with the coding of behavioral states. In line with previous single-unit data (*70*, *71*), this suggests that, as in the cortex (*58*, *59*), fast sensory dynamics and slow state dynamics can be orthogonally separated at the level of amygdala networks, which would allow for continuous population-level state encoding despite flexible

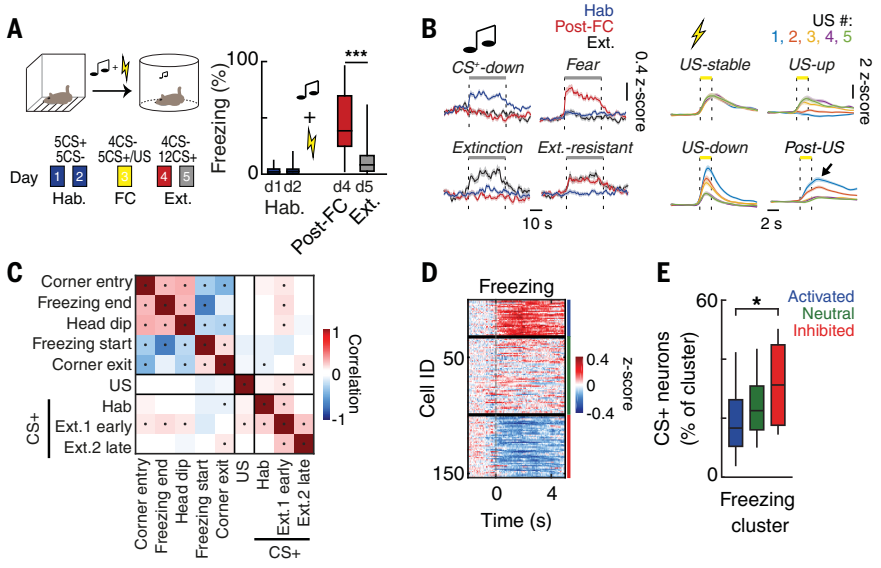

Fig. 5. Orthogonal representations of sensory stimuli and behavioral states. (**A**) Auditory FC paradigm and average CS+ freezing (post–FC freezing, 44 ± 6%; post–extinction freezing, 13 ± 3%; ***P < 0.001, Wilcoxon matched-pairs signed-rank test). Hab., habituation; Ext., extinction; d, day. (**B**) (Left) Average CS+ responses of CS-down, fear, extinction, and extinction-resistant neurons. (Right) Average US responses of US-stable, US-up, US-down, and post-US excited neurons. (**C**) Single-cell correlation matrix of behavioral responses as well as CS and US responses across animals (dots indicate significant correlations across animals). (**D**) Clustered freezing responses of 152 neurons of one example animal. The color bar indicates the z-score. (**E**) Average proportion of CS+ and freezing cluster–responsive neurons out of the total population [CS+ and freezing activated = 18 ± 4%, CS+ and freezing neutral = 24 ± 3%, CS+ and freezing inhibited = 32 ± 5%; *P(activated versus inhibited) = 0.029, Friedman test (P = 0.03, F = 6.89) with post hoc Dunn's multiple-comparison test]. Box-and-whisker plots indicate the median, the interquartile range, and the minimum to maximum values of the data distribution. All data are generated from n = 9 animals.

single-cell representations of sensory inputs (*72*). Additionally, biased representations of emotionally salient stimuli in freezing-inhibited neurons may represent possible circuit mechanisms to substantially increase the signal-to-noise ratio and enhance the animal's ability to rapidly and reliably select appropriate behavioral reactions when facing danger. Beyond freezing, the concurrent signaling of both the CS and the learned, conditioned responses (CRs) in the BA (*73*) would not only allow for a flexible, state-driven modulation of CS representations but also enable appropriate CR selection in a state-dependent manner.

Previous reports identified defined BA output pathways with specific behavioral functions (*35*–*37*, *74*, *75*). Correlations of responses to the behavioral state transitions were by and large conserved across major BA output pathways, including projections to the vHC, the NAc, and the mPFC, despite individual differences between CS and US coding in these projections. Although we cannot rule out projection-target differences of state coding in relation to local gamma entrainment (*67*), the interactions between BA state signals and defined up- and downstream ensembles remain unknown (*42*, *76*). Nevertheless, broadcasting of amygdala state signals to larger brain networks, including cortical and subcortical areas, is likely to play an important role for state-dependent regulation (*27*, *30*, *40*, *77*–*79*), with a potential to broadly modulate brain state (*2*, *59*) and internal drive and generally modify affective states and behaviors. Our findings extend the concept of classical thalamocortical brain-state coding toward affective and exploratory states and provide an entry point into the state dependency of brain function and behavior in defined brain circuits.

Materials and Methods

Animals and viruses

Male C57BL/6J mice (C57BL/6JRccHsd; Envigo) were used throughout the study. Viruses were purchased from Penn Vector Core (AAV2/5.CaMKII.GCaMP6f.WPRE.SV40; titer, 2.49 × 10^{13}/ml) or custom-made in the case of the retrograde adeno-associated virus (retroAAV) (*80*) (retroAAV.EF1a.GCaMP6f.WPRE; Georg Keller, FMI Vector Core; titer, 3.9 × 10^{11}/ml). rAAV2-retro helper was a gift from Alla Karpova and David Schaffer (Addgene plasmid 81070). retroAAV virus was supplemented with blue nonretrograde polymer microspheres (1:2400; Duke Scientific) to label injection sites. All animal experiments were performed in accordance with institutional guidelines and permitted by the authorities of the canton Basel-Stadt.

Surgeries

Eight-week-old male mice were anesthetized (with isoflurane) and placed in a stereotactic frame (Kopf Instruments). Three hundred nanoliters (for retroAAV.EF1a.GCaMP6f injection into the vHC, mPFC, or NAc) or 500 nl (for AAV2/5.CamKII.GCaMP6f injection into the BA) of virus was injected into the respective target area by using a glass pipette connected to a picospritzer during a stereotactic brain surgery under isoflurane anesthesia (1 to 2%). One week after virus injection, the animals underwent a second surgery for gradient refractive index (GRIN) lens implantation. An 800-μm-diameter craniotomy was drilled above the BA. Next, a small track was cut with a 0.7-mm sterile needle through the hole and cortex to aid GRIN lens insertion. A 600-μm-diameter GRIN lens (Inscopix) was then slowly advanced into the BA (–4.4 mm ventral to the pia surface). The GRIN lens was fixed to the skull with light curable glue (Loctite 4305; Henkel), and the skull was sealed with Scotchbond (3M), Vetbond (3M), and dental acrylic (Paladur; Kulzer). A custom-made head bar for animal fixation during miniature microscope mounting was attached. Animals were provided with analgesia (buprenorphine and ropivacaine), and their well-being was monitored throughout the experimental period.

Behavioral paradigm

Animals were single-housed on a 12-hour light cycle, and behavioral experiments were performed during the light period. Anxiety tests and FC were combined in the following manner on seven consecutive days: OF test, EPM test, habituation 1, habituation 2, FC, extinction 1, and extinction 2. The OF test was performed in a 40-cm by 40-cm by 40-cm plastic box with an evenly distributed light intensity of 24 lux. The EPM was composed of two orthogonal open and closed arms (30 cm each) and a center zone (6 cm) elevated at 55 cm above the ground. Mice were allowed to freely explore the OF and EPM for 10 to 15 min. Habituation and extinction experiments were performed in a 23-cm-diameter circular plexiglass arena. Mice were presented with 5 CS+ and 5 CS– stimuli (6 or 12 kHz, counterbalanced) during the habituation sessions and 4 CS– and 12 CS+ stimuli during the extinction session. The CS comprised 27 tone pips, each pip 200 ms in duration and 75 dB in amplitude, presented at a rate of 1.1 Hz (Tucker Davis Technologies, TDT 78). FC was performed in a 26-cm-wide square plexiglass context with a Coulbourn shock grid. After termination of the CS+, the mouse received a 2-s-long, 0.65-mA AC foot shock 1.1 s after the last tone pip. Behavioral experiments were performed and recorded by using Sort Client (2.7.0), Radiant (2.0.0), and CinePlex (3.4.1) software in combination with the CinePlex and MAP data acquisition systems (all Plexon). Animals were perfused with 4% paraformaldehyde in phosphate-buffered saline at the end of the behavioral experiment, and brain slices (150 μm thick) were cut with a vibratome (Leica) and visualized by confocal microscopy (with a Zeiss LSM700 instrument) to verify GRIN lens location and imaging sites. Animals that lacked detectable expression of

GCaMP6f (a genetically encoded calcium indicator) before baseplate mounting or that had off-target viral injections were excluded from analysis.

Imaging experiments

Ca^{2+}-imaging studies in freely moving mice were performed via the implanted GRIN lens by using a miniaturized microscope (nVista, V2, nVista HD 2.0.4; Inscopix) (*43*). Microscope baseplates were glued to the dental acrylic ~1 week before the experiment, and mice were habituated to the microscope attachment procedure before behavioral experiments. Miniature microscopes were mounted onto the mouse's head right before each behavioral experiment by using a custom mounting station. Images were acquired at 1024 pixels by 1024 pixels and at a frame rate of 20 Hz. Imaging parameters were set at 20 to 80% light-emitting diode (LED) intensity (0.4 to 1.7 mW, 473 nm) and a gain of 1 to 2 depending on GCaMP6f expression levels.

Data analysis

Behavior

Behavioral data were manually scored (for EPM head dips, defined as brief periods of distinct downward movement of the mouse's head over the edge of the open arms, and for OF rearing) or automatically tracked by top-down movies using CinePlex Studio and Editor software (Plexon). Freezing was assessed by using the two-dimensional (2D) motion data and Freezing Analysis plug-in of Editor (Plexon) (minimum absence of movement, 2 s, with the threshold adjusted on a case-by-case basis) combined with additional manual post hoc checks for nonfreezing but stationary behaviors (e.g., grooming). OF test and EPM 2D locations were tracked offline. OF locations were defined as follows: center, the center quarter of the OF area, and corners, $^{1}/_{16}$ of the OF area measured from each corner of the arena. Corner-entry and -exit times were detected as the animal's crossings of the corner area outlines (36 ± 7 transitions per animal) with a minimum time of 0.5 s in each area before and after the transition to exclude events that were nondirected outline crossings (e.g., lingering on the zone border). The number of corner transitions and EPM closed- and open-arm times, as well as center location times, were calculated by using Editor (Plexon) and Matlab.

Ca^{2+} imaging

Raw imaging movies were preprocessed and normalized by using a fast Fourier transform band-pass filter in ImageJ. For normalization, each image was divided by its filtered image. After preprocessing, the movies were spatially down-sampled by a factor of four. The movies of all individual experimental days were then concatenated and motion corrected across all frames in Matlab by using the TurboReg algorithm (*81*). Single-cell regions of interest (ROIs) were extracted by using a combination of principal components analysis and independent component analysis with post hoc independent component truncation at 50% peak intensity (*38*, *82*). ROI size was limited to a maximum diameter of 30 pixels (~60 μm). ROIs were then overlaid with a maximum-intensity projection of the raw movie and were excluded if they overlapped with noncellular components (e.g., the edge of the GRIN lens or blood vessels) or if multiple ROIs were detected for the same maximum-intensity projection of the same neuron. Pixels within ROIs were normalized and cut at 50% of the maximum ROI pixel intensity. Fluorescence traces for each ROI were extracted as the average pixel intensity within the normalized ROI projected along the filtered and motion-corrected 20-Hz raw fluorescence movie. Traces that failed to pass quality criteria upon visual inspection across sessions (those dominated by sharp, negative transients) were excluded. We typically retained 44% of ROIs [number of initial independent components (ICs), 300] after applying the above-mentioned exclusion criteria.

Before further analysis, linear trends across an entire session were removed from the Ca^{2+} traces and z-scores of the detrended traces were used as the activity traces for all further calculations.

Area scores

The area bias in single-neuron responses was calculated by using the average spatial activity map of each neuron: the total activity in a specific x-y location normalized by the total time the animal spent in that location. x-y data were discretized in 256 pixels and smoothed with a 2D Gaussian kernel that was $^{1}/_{64}$ the arena size. The difference between the total normalized activation in the corners (defined as above) and that in the center was used as a measure of the bias. We calculated the area score for all neurons in the dataset and set the threshold at 1 standard deviation around zero to capture the behavior of the distribution tails. This threshold was calculated once for the entire population of neurons and applied to each mouse. To create the temporally shifted dataset, behavioral time courses were circle-shifted by a random amount relative to the neuronal activity time course, and area scores were calculated for 1000 random shifts for each animal.

Area decoding

We used support vector classification with a quadratic kernel for all decoders. The animal location was determined in 1-s bins as center, corners, or walls according to the definitions above, and bins with nonconsistent behavior were excluded from analysis. To avoid very unbalanced designs, if an animal spent less than 15% of the session in the corner, the decoder was trained and tested on the times the mouse was either in the corner or in the center. Likewise, if the animal spent less than 15% of the session in the center, the animal location was defined as corner versus noncorner locations (center or walls) and the decoder was trained and tested on this distinction. To control for the local dependencies in both the behavioral data and the neuronal responses, we repeated the decoding training procedure with the behavior circularly rotated relative to the neuronal activity. Maintaining the signal's local structure resulted in a consistent modest drop in decoding performance that was highly significant (decoding performance on real data was higher than performance on shifted data in 99.8 ± 0.2% of all possible shifts) (see fig. S2L).

Neuronal response analysis and clustering

Single-neuron responses to corner entry were averaged for each neuron in a time window from 2 s before transition to 5 s after. The mean responses of all neurons from each animal were then clustered into three groups by using k-means clustering with Euclidean distance between the mean response traces as the distance measure. The result was a cluster of generally activated neurons (ensemble 1), a cluster of generally inhibited neurons (ensemble 2), and cells with weak or mixed responses (a neutral cluster) for each animal. The same procedure was used to define three functional ensembles on the basis of mean responses aligned to the freezing start period (Fig. 5D).

CS and US responses were analyzed by using a combined statistical and supervised cluster analysis. First, CS- and US-responsive cells were identified as significantly responsive if their binned Ca^{2+} fluorescence (CS, 1-s bins, ±30-s window around CS onset; US, 1-s bin, ±14-s window around US onset) during the stimulus was significantly increased (CS) as well as significantly increased or decreased (US) (Wilcoxon signed-rank test, alpha-level, 0.01) compared with baseline conditions in at least three or two stimulus presentations for the US or CS, respectively (on at least one experimental condition for CS responses). This minimum number of sensory responses allowed a reliable detection of CS and US plasticity profiles instead of merely general responsiveness across all days, without being too sensitive for random Ca^{2+} responses during individual tone presentations. Responses for the CS were collected to tones 1 to 5 in the two habituation sessions and in the first fear extinction session (Ext. early) and to tones 8 to 12 in the second fear extinction session (Ext. late). The average neuronal response across both habituation sessions was used as the habituation response of the cells. Next, we used a supervised clustering approach on the subset of significantly responsive cells to identify different subtypes of CS- and US-responsive neurons. Neuronal responses were collected in time windows of −2 s to 15 s and −10 s to 30 s around US and CS onset, respectively. Principal components analysis was performed on the concatenated responses to the five US stimuli in the FC session to identify the dynamics in the US responses within this session. Responses were then projected on the first four principle components (>60% variance explained), and k-means clustering was performed (k = 11, cosine distance). We then manually joined clusters with similar response profiles in relation to the six response

types described above (Fig. 5 and fig. S7). This procedure was replicated for the CS responses after averaging responses to the five selected tones in the habituation and extinction sessions as described above, to identify the different dynamics in CS responses along the conditioning paradigm (*36*, *38*).

Correlation analysis

Average responses aligned to the onset of different behaviors were calculated in the different sessions: corner entry (OF), corner exit (OF), freezing period start and end (habituation and extinction), and head dips (EPM). Response to freezing and corner entry or exit was quantified as the difference between the mean response in the 2-s time window starting 1 s after behavior onset (response) and the 2-s time window ending 1 s before onset (baseline). Head dip was quantified as the difference between the mean response in the 1-s time window starting 0.8 s before behavior detection (response) and the 1-s time window ending 1 s before behavior detection (baseline), because of the different dynamics of the behavior. CS and US responses were quantified with similar baseline periods, defined as the 2-s time window ending 1 s before stimulus onset, and a response period defined as the 2 s after onset (US) or the 9 s starting 1 s after onset (CS). Pearson's correlation was calculated between the neuronal responses to each pair of behaviors for each animal.

Statistics

Statistical analysis was performed with Prism 7 (GraphPad) and Matlab (Mathworks). Values are represented as the mean ± SEM unless stated otherwise. Box-and-whisker plots indicate the median, the interquartile range, and the minimum to maximum values of the data distribution. Normality of the data was not assumed, and all tests were nonparametric tests. Statistical tests and test statistics are mentioned in the text and figure legends. *, **, and *** indicate P values smaller than 0.05, 0.01, and 0.001, respectively.

REFERENCES AND NOTES

1. A. Kennedy *et al*., Internal states and behavioral decision-making: Toward an integration of emotion and cognition. *Cold Spring Harb. Symp. Quant. Biol.* **79**, 199–210 (2014). doi: 10.1101/sqb.2014.79.024984; pmid: 25948637
2. M. J. McGinley *et al*., Waking state: Rapid variations modulate neural and behavioral responses. *Neuron* **87**, 1143–1161 (2015). doi: 10.1016/j.neuron.2015.09.012; pmid: 26402600
3. J. F. A. Poulet, C. C. H. Petersen, Internal brain state regulates membrane potential synchrony in barrel cortex of behaving mice. *Nature* **454**, 881–885 (2008). doi: 10.1038/nature07150; pmid: 18633351
4. M. L. Schölvinck, A. B. Saleem, A. Benucci, K. D. Harris, M. Carandini, Cortical state determines global variability and correlations in visual cortex. *J. Neurosci.* **35**, 170–178 (2015). doi: 10.1523/JNEUROSCI.4994-13.2015; pmid: 25568112
5. M. Lovett-Barron *et al*., Ancestral circuits for the coordinated modulation of brain state. *Cell* **171**, 1411–1423.e17 (2017). doi: 10.1016/j.cell.2017.10.021; pmid: 29103613
6. S. H. Lee, Y. Dan, Neuromodulation of brain states. *Neuron* **76**, 209–222 (2012). doi: 10.1016/j.neuron.2012.09.012; pmid: 23040816
7. J. Gründemann, A. Lüthi, Ensemble coding in amygdala circuits for associative learning. *Curr. Opin. Neurobiol.* **35**, 200–206 (2015). doi: 10.1016/j.conb.2015.10.005; pmid: 26531780
8. D. J. Anderson, R. Adolphs, A framework for studying emotions across species. *Cell* **157**, 187–200 (2014). doi: 10.1016/j.cell.2014.03.003; pmid: 24679535
9. L. K. Allikmets, Behavioral reactions to electrical stimulation of amygdala in cats. *Neurosci. Transl.* **1**, 119–127 (1967). doi: 10.1007/BF01124389
10. J. Panksepp, Aggression elicited by electrical stimulation of the hypothalamus in albino rats. *Physiol. Behav.* **6**, 321–329 (1971). doi: 10.1016/0031-9384(71)90163-6; pmid: 4948212
11. J. P. Fadok *et al*., A competitive inhibitory circuit for selection of active and passive fear responses. *Nature* **542**, 96–100 (2017). doi: 10.1038/nature21047; pmid: 28117439
12. D. Lin *et al*., Functional identification of an aggression locus in the mouse hypothalamus. *Nature* **470**, 221–226 (2011). doi: 10.1038/nature09736; pmid: 21307935
13. J. N. Betley *et al*., Neurons for hunger and thirst transmit a negative-valence teaching signal. *Nature* **521**, 180–185 (2015). doi: 10.1038/nature14416; pmid: 25915020
14. E. H. Nieh *et al*., Inhibitory input from the lateral hypothalamus to the ventral tegmental area disinhibits dopamine neurons and promotes behavioral activation. *Neuron* **90**, 1286–1298 (2016). doi: 10.1016/j.neuron.2016.04.035; pmid: 27238864
15. A. M. Douglass *et al*., Central amygdala circuits modulate food consumption through a positive-valence mechanism. *Nat. Neurosci.* **20**, 1384–1394 (2017). doi: 10.1038/nn.4623; pmid: 28825719
16. J. H. Jennings, G. Rizzi, A. M. Stamatakis, R. L. Ung, G. D. Stuber, The inhibitory circuit architecture of the lateral hypothalamus orchestrates feeding. *Science* **341**, 1517–1521 (2013). doi: 10.1126/science.1241812; pmid: 24072922
17. R. J. Blanchard *et al*., Behavioral and endocrine change following chronic predatory stress. *Physiol. Behav.* **63**, 561–569 (1998). doi: 10.1016/S0031-9384(97)00508-8; pmid: 9523899
18. L. S. Lester, M. S. Fanselow, Exposure to a cat produces opioid analgesia in rats. *Behav. Neurosci.* **99**, 756–759 (1985). doi: 10.1037/0735-7044.99.4.756; pmid: 3843739
19. V. P. Bakshi, K. M. Alsene, P. H. Roseboom, E. E. Connors, Enduring sensorimotor gating abnormalities following predator exposure or corticotropin-releasing factor in rats: A model for PTSD-like information-processing deficits? *Neuropharmacology* **62**, 737–748 (2012). doi: 10.1016/j.neuropharm.2011.01.040; pmid: 21288473
20. R. Adamec, D. Fougere, V. Risbrough, CRF receptor blockade prevents initiation and consolidation of stress effects on affect in the predator stress model of PTSD. *Int. J. Neuropsychopharmacol.* **13**, 747–757 (2010). doi: 10.1017/S1461145709990496; pmid: 19751543
21. A. K. Rajbhandari, B. A. Baldo, V. P. Bakshi, Predator stress-induced CRF release causes enduring sensitization of basolateral amygdala norepinephrine systems that promote PTSD-like startle abnormalities. *J. Neurosci.* **35**, 14270–14285 (2015). doi: 10.1523/JNEUROSCI.5080-14.2015; pmid: 26490866
22. R. E. Adamec, T. Shallow, Lasting effects on rodent anxiety of a single exposure to a cat. *Physiol. Behav.* **54**, 101–109 (1993). doi: 10.1016/0031-9384(93)90050-P; pmid: 8327588
23. R. J. Blanchard, D. C. Blanchard, Defensive reactions in the albino rat. *Learn. Motiv.* **2**, 351–362 (1971). doi: 10.1016/0023-9690(71)90016-6
24. C. D. Salzman, S. Fusi, Emotion, cognition, and mental state representation in amygdala and prefrontal cortex. *Annu. Rev. Neurosci.* **33**, 173–202 (2010). doi: 10.1146/annurev.neuro.051508.135256; pmid: 20331363
25. Y. Li *et al*., Neuronal representation of social information in the medial amygdala of awake behaving mice. *Cell* **171**, 1176–1190. e17 (2017). doi: 10.1016/j.cell.2017.10.015; pmid: 29107332
26. R. Remedios *et al*., Social behaviour shapes hypothalamic neural ensemble representations of conspecific sex. *Nature* **550**, 388–392 (2017). doi: 10.1038/nature23885; pmid: 29052632
27. P. Tovote *et al*., Midbrain circuits for defensive behaviour. *Nature* **534**, 206–212 (2016). doi: 10.1038/nature17996; pmid: 27279213
28. Y. Yang *et al*., Selective synaptic remodeling of amygdalocortical connections associated with fear memory. *Nat. Neurosci.* **19**, 1348–1355 (2016). doi: 10.1038/nn.4370; pmid: 27595384
29. J. E. Krettek, J. L. Price, Projections from the amygdaloid complex to the cerebral cortex and thalamus in the rat and cat. *J. Comp. Neurol.* **172**, 687–722 (1977). doi: 10.1002/cne.901720408; pmid: 838895
30. R. D. Stith, R. J. Person, R. C. Dana, Effects of hippocampal and amygdalar stimulation on uptake and binding of 3H-hydrocortisone in the hypothalamus of the cat. *J. Neurosci. Res.* **2**, 317–322 (1976). doi: 10.1002/jnr.490020409; pmid: 1011302
31. M. T. Rogan, U. V. Stäubli, J. E. LeDoux, Fear conditioning induces associative long-term potentiation in the amygdala. *Nature* **390**, 604–607 (1997). doi: 10.1038/37601; pmid: 9403688
32. M. A. Belova, J. J. Paton, S. E. Morrison, C. D. Salzman, Expectation modulates neural responses to pleasant and aversive stimuli in primate amygdala. *Neuron* **55**, 970–984 (2007). doi: 10.1016/j.neuron.2007.08.004; pmid: 17880899
33. J. J. Paton, M. A. Belova, S. E. Morrison, C. D. Salzman, The primate amygdala represents the positive and negative value of visual stimuli during learning. *Nature* **439**, 865–870 (2006). doi: 10.1038/nature04490; pmid: 16482160
34. B. J. Everitt, R. N. Cardinal, J. A. Parkinson, T. W. Robbins, Appetitive behavior: Impact of amygdala-dependent mechanisms of emotional learning. *Ann. N.Y. Acad. Sci.* **985**, 233–250 (2003). doi: 10.1111/j.1749-6632.2003.tb07085.x; pmid: 12724162
35. V. Senn *et al*., Long-range connectivity defines behavioral specificity of amygdala neurons. *Neuron* **81**, 428–437 (2014). doi: 10.1016/j.neuron.2013.11.006; pmid: 24462103
36. C. Herry *et al*., Switching on and off fear by distinct neuronal circuits. *Nature* **454**, 600–606 (2008). doi: 10.1038/nature07166; pmid: 18615015
37. P. Namburi *et al*., A circuit mechanism for differentiating positive and negative associations. *Nature* **520**, 675–678 (2015). doi: 10.1038/nature14366; pmid: 25925480
38. B. F. Grewe *et al*., Neural ensemble dynamics underlying a long-term associative memory. *Nature* **543**, 670–675 (2017). doi: 10.1038/nature21682; pmid: 28329757
39. S.-C. Lee, A. Amir, D. Haufler, D. Pare, Differential recruitment of competing valence-related amygdala networks during anxiety. *Neuron* **96**, 81–88.e5 (2017). doi: 10.1016/j.neuron.2017.09.002; pmid: 28957678
40. A. Amir, S.-C. Lee, D. B. Headley, M. M. Herzallah, D. Pare, Amygdala signaling during foraging in a hazardous environment. *J. Neurosci.* **35**, 12994–13005 (2015). doi: 10.1523/JNEUROSCI.0407-15.2015; pmid: 26400931
41. E. J. Kim *et al*., Dynamic coding of predatory information between the prelimbic cortex and lateral amygdala in foraging rats. *Sci. Adv.* **4**, eaar7328 (2018). doi: 10.1126/sciadv.aar7328; pmid: 29675471
42. E. Likhtik, J. M. Stujenske, M. A. Topiwala, A. Z. Harris, J. A. Gordon, Prefrontal entrainment of amygdala activity signals safety in learned fear and innate anxiety. *Nat. Neurosci.* **17**, 106–113 (2014). doi: 10.1038/nn.3582; pmid: 24241397
43. K. K. Ghosh *et al*., Miniaturized integration of a fluorescence microscope. *Nat. Methods* **8**, 871–878 (2011). doi: 10.1038/nmeth.1694; pmid: 21909102
44. R. G. Lister, The use of a plus-maze to measure anxiety in the mouse. *Psychopharmacology* **92**, 180–185 (1987). doi: 10.1007/BF00177912; pmid: 3110839
45. L. Prut, C. Belzung, The open field as a paradigm to measure the effects of drugs on anxiety-like behaviors: A review. *Eur. J. Pharmacol.* **463**, 3–33 (2003). doi: 10.1016/S0014-2999(03)01272-X; pmid: 12600700
46. P. Botta *et al*., Regulating anxiety with extrasynaptic inhibition. *Nat. Neurosci.* **18**, 1493–1500 (2015). doi: 10.1038/nn.4102; pmid: 26322928
47. K. M. Tye *et al*., Amygdala circuitry mediating reversible and bidirectional control of anxiety. *Nature* **471**, 358–362 (2011). doi: 10.1038/nature09820; pmid: 21389985
48. A. Dalvi, R. J. Rodgers, Behavioral effects of diazepam in the murine plus-maze: Flumazenil antagonism of enhanced head dipping but not the disinhibition of open-arm avoidance. *Pharmacol. Biochem. Behav.* **62**, 727–734 (1999). doi: 10.1016/S0091-3057(98)00220-2; pmid: 10208379
49. A. Beyeler *et al*., Divergent routing of positive and negative information from the amygdala during memory retrieval. *Neuron* **90**, 348–361 (2016). doi: 10.1016/j.neuron.2016.03.004; pmid: 27041499
50. D. C. Anderson, C. Crowell, D. Koehn, J. V. Lupo, Different intensities of unsignalled inescapable shock treatments as determinants of non-shock-motivated open field behavior: A resolution of disparate results. *Physiol. Behav.* **17**, 391–394 (1976). doi: 10.1016/0031-9384(76)90096-2; pmid: 1013183
51. E. H. Y. Lee, M. J. Tsai, C. Y. Chai, Stress selectively influences center region activity of mice in an open field. *Physiol. Behav.* **37**, 659–662 (1986). doi: 10.1016/0031-9384(86)90301-X; pmid: 3749331

52. P. Simon, R. Dupuis, J. Costentin, Thigmotaxis as an index of anxiety in mice. Influence of dopaminergic transmissions. *Behav. Brain Res.* **61**, 59–64 (1994). doi: 10.1016/0166-4328(94)90008-6; pmid: 7913324
53. F. J. Helmstetter, Stress-induced hypoalgesia and defensive freezing are attenuated by application of diazepam to the amygdala. *Pharmacol. Biochem. Behav.* **44**, 433–438 (1993). doi: 10.1016/0091-3057(93)90487-E; pmid: 8446677
54. L. H. Conti, C. R. Maciver, J. W. Ferkany, M. E. Abreu, Footshock-induced freezing behavior in rats as a model for assessing anxiolytics. *Psychopharmacology* **102**, 492–497 (1990). doi: 10.1007/BF02247130; pmid: 1982903
55. T. Inoue, K. Tsuchiya, T. Koyama, Serotonergic activation reduces defensive freezing in the conditioned fear paradigm. *Pharmacol. Biochem. Behav.* **53**, 825–831 (1996). doi: 10.1016/0091-3057(95)02084-5; pmid: 8801584
56. Y. Maki *et al*., Monoamine oxidase inhibitors reduce conditioned fear stress-induced freezing behavior in rats. *Eur. J. Pharmacol.* **406**, 411–418 (2000). doi: 10.1016/S0014-2999(00)00706-8; pmid: 11040348
57. K. D. Harris, A. Thiele, Cortical state and attention. *Nat. Rev. Neurosci.* **12**, 509–523 (2011). doi: 10.1038/nrn3084; pmid: 21829219
58. S. Musall, M. T. Kaufman, S. Gluf, A. K. Churchland, Movement-related activity dominates cortex during sensory-guided decision making. bioRxiv 308288 [Preprint]. 10 May 2018. doi: 10.1101/308288
59. C. Stringer, M. Pachitariu, N. Steinmetz, C. B. Reddy, M. Carandini, K. D. Harris, Spontaneous behaviors drive multidimensional, brain-wide population activity. bioRxiv 306019. 28 December 2018. doi: 10.1101/306019
60. P. O. Polack, J. Friedman, P. Golshani, Cellular mechanisms of brain state-dependent gain modulation in visual cortex. *Nat. Neurosci.* **16**, 1331–1339 (2013). doi: 10.1038/nn.3464; pmid: 23872595
61. J. Reimer *et al*., Pupil fluctuations track fast switching of cortical states during quiet wakefulness. *Neuron* **84**, 355–362 (2014). doi: 10.1016/j.neuron.2014.09.033; pmid: 25374359
62. T. A. Engel *et al*., Selective modulation of cortical state during spatial attention. *Science* **354**, 1140–1144 (2016). doi: 10.1126/science.aag1420; pmid: 27934763
63. C. M. Niell, M. P. Stryker, Modulation of visual responses by behavioral state in mouse visual cortex. *Neuron* **65**, 472–479 (2010). doi: 10.1016/j.neuron.2010.01.033; pmid: 20188652
64. E. Vogel, S. Krabbe, J. Gründemann, J. I. Wamsteeker Cusulin, A. Lüthi, Projection-specific dynamic regulation of inhibition in amygdala micro-circuits. *Neuron* **91**, 644–651 (2016). doi: 10.1016/j.neuron.2016.06.036; pmid: 27497223
65. C. K. Machens, R. Romo, C. D. Brody, Flexible control of mutual inhibition: A neural model of two-interval discrimination. *Science* **307**, 1121–1124 (2005). doi: 10.1126/science.1104171; pmid: 15718474
66. J. Kim, M. Pignatelli, S. Xu, S. Itohara, S. Tonegawa, Antagonistic negative and positive neurons of the basolateral amygdala. *Nat. Neurosci.* **19**, 1636–1646 (2016). doi: 10.1038/nn.4414; pmid: 27749826
67. A. Amir, D. B. Headley, S.-C. Lee, D. Haufler, D. Paré, Vigilance-associated gamma oscillations coordinate the ensemble activity of basolateral amygdala neurons. *Neuron* **97**, 656–669. e7 (2018). doi: 10.1016/j.neuron.2017.12.035; pmid: 29420934
68. T. Amano, S. Duvarci, D. Popa, D. Paré, The fear circuit revisited: Contributions of the basal amygdala nuclei to conditioned fear. *J. Neurosci.* **31**, 15481–15489 (2011). doi: 10.1523/JNEUROSCI.3410-11.2011; pmid: 22031894
69. G. J. Quirk, C. Repa, J. E. LeDoux, Fear conditioning enhances short-latency auditory responses of lateral amygdala neurons: Parallel recordings in the freely behaving rat. *Neuron* **15**, 1029–1039 (1995). doi: 10.1016/0896-6273(95)90092-6; pmid: 7576647
70. K. A. Goosens, J. A. Hobin, S. Maren, Auditory-evoked spike firing in the lateral amygdala and Pavlovian fear conditioning: Mnemonic code or fear bias? *Neuron* **40**, 1013–1022 (2003). doi: 10.1016/S0896-6273(03)00728-1; pmid: 14659099
71. D. Paré, D. R. Collins, Neuronal correlates of fear in the lateral amygdala: Multiple extracellular recordings in conscious cats. *J. Neurosci.* **20**, 2701–2710 (2000). doi: 10.1523/JNEUROSCI.20-07-02701.2000; pmid: 10729351
72. S. Druckmann, D. B. Chklovskii, Neuronal circuits underlying persistent representations despite time varying activity. *Curr. Biol.* **22**, 2095–2103 (2012). doi: 10.1016/j.cub.2012.08.058; pmid: 23084992
73. P. Kyriazi, D. B. Headley, D. Pare, Multi-dimensional coding by basolateral amygdala neurons. *Neuron* **99**, 1315–1328.e5 (2018). doi: 10.1016/j.neuron.2018.07.036
74. E. H. Nieh, S.-Y. Kim, P. Namburi, K. M. Tye, Optogenetic dissection of neural circuits underlying emotional valence and motivated behaviors. *Brain Res.* **1511**, 73–92 (2013). doi: 10.1016/j.brainres.2012.11.001; pmid: 23142759
75. A. C. Felix-Ortiz, K. M. Tye, Amygdala inputs to the ventral hippocampus bidirectionally modulate social behavior. *J. Neurosci.* **34**, 586–595 (2014). doi: 10.1523/JNEUROSCI.4257-13.2014; pmid: 24403157
76. J. M. Stujenske, E. Likhtik, M. A. Topiwala, J. A. Gordon, Fear and safety engage competing patterns of theta-gamma coupling in the basolateral amygdala. *Neuron* **83**, 919–933 (2014). doi: 10.1016/j.neuron.2014.07.026; pmid: 25144877
77. K. M. Tye, P. H. Janak, Amygdala neurons differentially encode motivation and reinforcement. *J. Neurosci.* **27**, 3937–3945 (2007). doi: 10.1523/JNEUROSCI.5281-06.2007; pmid: 17428967
78. A. C. Felix-Ortiz *et al*., BLA to vHPC inputs modulate anxiety-related behaviors. *Neuron* **79**, 658–664 (2013). doi: 10.1016/j.neuron.2013.06.016; pmid: 23972595
79. R. Paz, J. G. Pelletier, E. P. Bauer, D. Paré, Emotional enhancement of memory via amygdala-driven facilitation of rhinal interactions. *Nat. Neurosci.* **9**, 1321–1329 (2006). doi: 10.1038/nn1771; pmid: 16964249
80. D. G. R. Tervo *et al*., A designer AAV variant permits efficient retrograde access to projection neurons. *Neuron* **92**, 372–382 (2016). doi: 10.1016/j.neuron.2016.09.021; pmid: 27720486
81. P. Thévenaz, U. E. Ruttimann, M. Unser, A pyramid approach to subpixel registration based on intensity. *IEEE Trans. Image Process.* **7**, 27–41 (1998). doi: 10.1109/83.650848; pmid: 18267377
82. E. A. Mukamel, A. Nimmerjahn, M. J. Schnitzer, Automated analysis of cellular signals from large-scale calcium imaging data. *Neuron* **63**, 747–760 (2009). doi: 10.1016/j.neuron.2009.08.009; pmid: 19778505
83. G. Paxinos, K. Franklin, *Paxinos and Franklin's the Mouse Brain in Stereotaxic Coordinates* (Academic Press, 2012).

ACKNOWLEDGMENTS

We thank G. Keller and D. Gerosa Erni for virus production and V. Jayaraman, R. Kerr, D. Kim, L. Looger, K. Svoboda, and the HHMI Janelia GENIE Project for making GCaMP6 available, as well as A. Karpova and D. Schaffer, who gifted the rAAV2-retro helper (Addgene plasmid 81070V). We thank P. Argast and P. Buchmann for workshop and engineering support. **Funding:** Research was supported by the Swiss National Science Foundation (core grant to A.L., Ambizione Fellowship to J.G., SNF professorship to J.G., and Sinergia to B.F.G.), EMBO and Marie Curie Actions (J.G.), Brain & Behavior Research Foundation (NARSAD Young Investigator awards to S.K. and B.F.G.), Swiss Data Science Center (B.F.G.), DARPA (M.J.S.), NIH (M.J.S.), ERC (advanced grant to A.L.), and Novartis Research Foundation. **Author contributions:** J.G., Y.B., and A.L. designed experiments and analysis. J.G., T.L., and S.K. performed experiments. J.G., B.F.G., and M.J.S. established the Ca^{2+}-imaging protocol, experiments, and image data analysis. Y.B. and J.G. analyzed data. J.G., Y.B., and A.L. wrote the paper, and all authors edited the paper and commented on the manuscript. **Competing interests:** M.J.S. is a scientific co-founder of Inscopix, which produces the miniature fluorescence microscope used in this study. **Data and materials availability:** All data and analyses necessary to understand and assess the conclusions of the manuscript are presented in the main text and in the supplementary materials. Additional data relating to this paper are available upon request, owing to the size (35 TB) of the data.

SUPPLEMENTARY MATERIALS

science.sciencemag.org/content/364/6437/eaav8736/suppl/DC1
Figs. S1 to S11

28 October 2018; accepted 22 February 2019
10.1126/science.aav8736